Journal of Power Sources 524 (2022) 231084

Contents lists available at ScienceDirect

Journal of Power Sources

journal homepage: www.elsevier.com/locate/jpowsour

Interplay between coordination, dynamics, and conductivity mechanism in Mg/Al-catenated ionic liquid electrolytes

Gioele Pagot [a,b,c], Mounesha Garaga [c], Ankur L. Jadhav [d], Lauren F. O'Donnell [c], Keti Vezzù [a], Boris Itin [e], Robert J. Messinger [d], Steven G. Greenbaum [c,**], Vito Di Noto [a,b,*]

[a] Section of Chemistry for the Technology (ChemTech), Department of Industrial Engineering, University of Padova, Via Marzolo 9, I-35131, Padova, PD, Italy
[b] Centro Studi di Economia e Tecnica dell'Energia Giorgio Levi Cases, Via Marzolo 9, I-35131, Padova, PD, Italy
[c] Department of Physics & Astronomy, Hunter College of the City University of New York, 695 Park Avenue, 10065, New York, NY, United States
[d] Department of Chemical Engineering, The City College of New York, CUNY, 160 Convent Avenue, 10031, New York, NY, United States
[e] New York Structural Biology Center, 89 Convent Avenue, 10027, New York, NY, United States

HIGHLIGHTS

- Ion speciation and dynamics in IL electrolytes for multivalent metal batteries.
- ^{27}Al and ^{25}Mg NMR demonstrates the formation of anionic aggregates.
- Broadband electrical spectroscopy elucidates the conductivity mechanism.
- ^{1}H PFG-NMR reveals the coupling of dynamics of cation and anion aggregates.

GRAPHICAL ABSTRACT

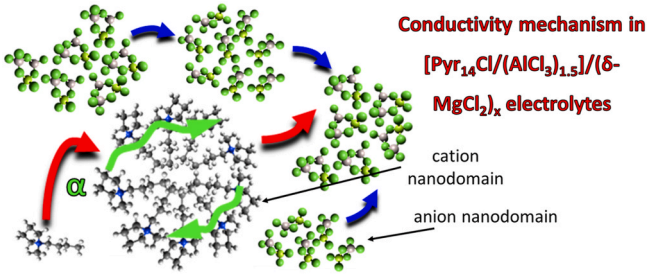

ARTICLE INFO

Keywords:
Al/Mg mixed metal batteries
Ionic liquids
Pulse-field-gradient (PFG)-NMR ^{27}Al and ^{25}Mg NMR
Broadband electrical spectroscopy (BES)
Ion dynamics

ABSTRACT

The development of batteries based on alternatives to lithium is essential to sustaining the increasing global energy demand. Earth abundant, energy dense metal anodes with mixed multivalent ions (*e.g.*, Mg/Al) are promising next-generation systems. A critical challenge, however, is the development of advanced electrolytes that are compatible with them. To achieve this target, a deeper understanding of their properties and conductivity mechanisms is needed. Herein, in a family of Al/Mg mixed metal ionic liquid-based electrolytes for secondary batteries, the ion-speciation, thermal behavior and long-range charge-migration processes is studied. It is revealed that the chemical compositions and temperature modulate the distribution of $AlCl_4^-$ and $Al_2Cl_7^-$ species in the anionic nanoaggregates of materials. These modifications are responsible of the mobility of ions, which is studied in detail by means of broadband electrical spectroscopy and pulse-field-gradient NMR. Results yield a clear picture of the role of ion aggregates in the long-range charge-migration processes occurring in these electrolytes.

* Corresponding author. Section of Chemistry for the Technology (ChemTech), Department of Industrial Engineering, University of Padova, Via Marzolo 9, I-35131, Padova, PD, Italy.
** Corresponding author.
E-mail addresses: steve.greenbaum@hunter.cuny.edu (S.G. Greenbaum), vito.dinoto@unipd.it (V. Di Noto).

https://doi.org/10.1016/j.jpowsour.2022.231084
Received 4 December 2021; Received in revised form 19 January 2022; Accepted 24 January 2022

1. Introduction

Ionic liquids (ILs) have attracted the attention of scientists due to their unique and tunable physicochemical properties originated by the intricate interplay of hydrogen bonding, coulombic and van-der-Waals interactions. Such unique properties include: (i) melting point; (ii) viscosity; (iii) density; (iv) solubility; and (v) hydrophobicity. An infinite number of different ILs can be synthesized by combining appropriate cations and anions, as well as by modulating the nature and the length of the alkyl functionalities bonded either to the cation or to the anion. Owing to these tunable properties, ILs find their application in a wide range of chemical fields, such as: (i) catalysis [1,2]; (ii) chemical separations [3]; (iii) organic synthesis [2]; (iv) metal extraction processes [4]; and (v) synthesis of inorganic nanomaterials [5]. More recently, ILs have been used as solvents or plasticizers in electrolytes for lithium [6–9], magnesium [10–15] and aluminum [16,17] secondary batteries. Indeed, ILs are preferred over conventional organic solvents due to their high thermal and electrochemical stability, high ionic conductivity, and efficient solvating power. Interestingly, when different metal salts are dissolved in conventional organic solvents (*e.g.*, diglyme and tetraglyme) thus obtaining binary or ternary $M_1^{x+}/M_2^{y+}/M_3^{z+}$ electrolytes (with M_n = Li, Mg, Al) [18,19], the only metal which is plated is magnesium. Indeed, it is demonstrated that the co-metal ions, *i.e.*, Li^+ and Al^{3+} in this case, are not electrodeposited. On the contrary, when unconventional IL-based electrolytes are exploited, it is possible to concurrently electrochemically deposit the two metals (*i.e.*, Mg and Al or Ti), as widely experimentally demonstrated [10,11,13,20]. Having an electrolyte able to co-deposit Mg^{2+} and Al^{3+}, for example, at the same potential, unlocks the possibility to obtain a hybrid Al/Mg battery endowed with an exceptional specific energy, given by both the high specific capacity of the three- and two-electron exchange of the two multivalent metals (*i.e.*, Al^{3+} and Mg^{2+}) and the low reduction potential set by magnesium (*i.e.*, −2.37 V *vs.* SHE).

Despite significant efforts on revealing the structure and interactions of species composing IL-based electrolytes, only relatively few works in the literature investigate the complex dynamics occurring in these systems, particularly over multiple time scales [21–23]. In this concern, the combination of Broadband Electrical Spectroscopy (BES) and Nuclear Magnetic Resonance spectroscopy (NMR) techniques is a powerful tool to achieve a comprehensive understanding of the processes controlling the long-range ion transport in electrolytes. Indeed, the electric response of IL-based materials, evaluated by BES studies, can give information on the ion conductivity mechanism in terms of polarization phenomena and dielectric relaxation events [24–31]. On the other hand, temperature-dependent single-pulse NMR and pulsed-field-gradient (PFG) NMR can reveal the dynamics and ion diffusivity mechanisms occurring in ion-conducting systems [32–36]. The obtained information is critical for the development of advanced materials for the energy storage technology field. In addition, there is still a controversial attribution of the equilibria existing between the different ionic species composing the IL-based systems, whose understanding is fundamental for the elucidation of the conductivity mechanism [37–39].

Herein, ion dynamics occurring in an Al/Mg hybrid multivalent metal conducting IL-based family of electrolytes for battery applications is deeply analyzed combining BES and NMR techniques. The materials consist of $AlCl_3$, 1-butyl-1-methylpyrrolidinium chloride ($Pyr_{14}Cl$) and δ-$MgCl_2$ in a molar ratio 1.5:1:x, with x = 0, 0.056, 0.091 and 0.146. Studies are gauged as a function of temperature and Mg concentration, demonstrating how the ionic composition and conductivity mechanism are modulated by these two variables. This work for the first time provides the tools to better understand ion speciation and long-range ion diffusion processes in this class of materials, thus opening the door to the development of high performing electrolytes for advanced Mg/Al mixed metal batteries.

2. Materials and methods

2.1. Materials preparation

1-Butyl-1-methylpyrrolidinium chloride (IoLiTec), $Pyr_{14}Cl$, was dried under vacuum at 105 °C for 7 days before use. Aluminum trichloride, magnesium (50 mesh), and 1-chlorobutane were Sigma Aldrich reagents. 1-chlorobutane was kept under Argon on molecular sieves. All the manipulations and reactions were performed under a strictly inert atmosphere (Ar or N_2), by means of a Schlenk line setup, or a glovebox. δ-$MgCl_2$ was prepared following a direct reaction between magnesium and 1-chlorobutane [40]. $Pyr_{14}Cl/(AlCl_3)_{1.5}$ (IL sample) was obtained by reacting $AlCl_3$ with $Pyr_{14}Cl$ in a molar ratio of 1.5:1 [20]. δ-$MgCl_2$ was dissolved in the IL sample up to a composition of $[Pyr_{14}Cl/(AlCl_3)_{1.5}]/(\delta\text{-}MgCl_2)_{0.146}$, and this solution was stirred for 2 h. Two intermediate $[Pyr_{14}Cl/(AlCl_3)_{1.5}]/(\delta\text{-}MgCl_2)_x$ samples (x = 0.056, 0.091) were prepared by dilution of $[Pyr_{14}Cl/(AlCl_3)_{1.5}]/(\delta\text{-}MgCl_2)_{0.146}$ electrolyte with appropriate amounts of IL.

2.2. Electrochemical studies

Electrochemical deposition and stripping processes obtained with $[Pyr_{14}Cl/(AlCl_3)_{1.5}]/(\delta\text{-}MgCl_2)_{0.056}$ sample were demonstrated by means of cyclic voltammetry (CV) experiments, collected using a VSP Bio-Logic potentiostat/galvanostat. Measurements were acquired at room temperature, using a three-electrodes electrochemical cell (Pt working electrode (WE), Mg counter electrode (CE) and Mg reference electrode (RE)).

2.3. NMR measurements

Solution-state ^{27}Al NMR spectra were acquired on a Varian Unity-500 spectrometer with a 11.7 T magnet operating at 130.318 MHz for ^{27}Al. A single-pulse sequence was employed with a 90° pulse of 11.6 μs and a recycle delay of 1 s. All samples were sealed in standard NMR 5-mm tube within an argon-filled glovebox (<1 ppm of H_2O and O_2). NMR experiments were conducted at 20, 40 and 60 °C. A 1.0 M $AlCl_3$ in D_2O (99.9 atom % D, Sigma-Aldrich) solution was used as reference for ^{27}Al nucleus. ^{25}Mg NMR spectra were obtained on a Bruker AVANCE NEO 750 MHz (17.62 T) wide bore UltraStabilized spectrometer operating at 45.91 MHz. A Hahn echo short gap non rotor-synchronized pulse sequence was employed in order to reduce the background noise. 90° and 180° pulse-lengths of 8 and 16 μs, respectively, were used for ^{25}Mg NMR measurements with a recycle delay of 0.1 s. For solid-state measurements, samples were packed in 4 mm zirconia rotors which were hermetically sealed under Ar using Kel-F drive tips. An aqueous solution of 11 M $MgCl_2$ was used as an external reference. A temperature range between 0 and 80 °C was investigated with an interval of 20 °C. The temperature was calibrated monitoring the chemical shift variation of lead nitrate as standard. ^1H PFG-NMR diffusion studies were acquired on a 7.05 T (300 MHz) Varian-S Direct Drive Wide Bore spectrometer equipped with a z-gradient probe (DOTY Scientific, Inc.) and using a stimulated-echo PFG sequence. Sixteen field gradient values were linearly increased from 5 and up to 1000 G cm^{-1}. Field gradient pulse durations (δ) of 2 ms and diffusion delays (Δ) of 0.1 s were used. The same instrument was used to perform the 1D ^1H NMR studies. 1D ^{27}Al and ^{25}Mg NMR curves were deconvoluted and quantitatively analyzed using the DMfit software [41].

2.4. Thermal measurements

The modulated differential scanning calorimetry (MDSC) analyses were carried out using a MDSC2920 (TA Instruments) furnished with a liquid nitrogen cooling system (heating ramp of 10 °C min^{-1} in the temperature range from −120 to 100 °C). Samples were hermetically sealed into aluminum pans to avoid moisture contamination.

2.5. Electrical measurements

The electric response of the electrolytes was studied by means of broadband electrical spectroscopy (BES) technique with a Novocontrol Alpha-A Analyzer. Data were collected every 10 °C between −100 and 150 °C, with an accuracy greater than ±0.2 °C, and in the frequency range from 30 mHz to 10 MHz. Samples, sandwiched between two platinum electrodes (13 mm diameter), were sealed into a home-made Teflon cell [10,31]. An optical fiber (d = 0.126 mm) was inserted between the two electrodes in order to keep constant the thickness of the samples and to prevent short circuits.

3. Results and discussion

The ability of these electrolytes to deposit and strip a Mg/Al alloy is proved by means of cyclic voltammetry studies using $[Pyr_{14}Cl/(AlCl_3)_{1.5}]/(\delta\text{-}MgCl_2)_{0.056}$ sample as representative material (see Fig. S1 in the Supporting Information). Further studies on the electrochemical properties of these materials, such as battery tests, Coulombic efficiency, long-term polarization and elemental composition of the electrodeposited alloy can be found in our previously published paper [20]. Results and data from the literature demonstrate that this electrolyte is able to deposit the Mg/Al alloy with a very low deposition overpotential (*ca.* −50 mV *vs.* Mg/Mg^{2+}), which is an outstanding value that ensures low ohmic drops and a high theoretical energy density when used in a real battery device. Moreover, in this experiment the aluminum electrodeposition process appears at a lower potential than expected value (*i.e.*, −2.37 rather than −1.66 V *vs.* SHE). It has been demonstrated that the downshift of the Al plating potential is the result of the presence of magnesium ions, which promotes the co-deposition process of this alloy [20]. After the deposition, Al and Mg are then efficiently stripped during the oxidation process, exhibiting a remarkable current density (*i.e.*, *ca.* 7 mA cm^{-2}). No shoulders are observed in the CV curve, excluding the presence of more than one independent redox event and thus indicating that both Al and Mg are deposited and stripped simultaneously during the same electrochemical event. Taking all together, these results indicate that the proposed class of materials are suitable for the application in hybrid Al/Mg multivalent metal batteries, where the two metals concurrently work as active ions during the operation of the battery. In this concern, a more detailed description of the ion speciation and long-range ion diffusion processes occurring using these electrolytes is necessary to comprehend and further improve their performance.

3.1. Ionic speciation

It is reported that, in "*Lewis acidic*" aluminum chloride-based ILs (*i.e.*, when $AlCl_3$:Cl is over 1.0) chloroaluminate anions form concatenated anionic domains by connecting through Cl^- bridges two different building blocks, *i.e.*, the monomer $AlCl_4^-$ and the dimer $Al_2Cl_7^-$ [10,38,39]. When δ-$MgCl_2$ is dissolved into these systems, catenated $[AlCl_4^-\text{-}MgCl_2]_n$ and $[Al_2Cl_7^-\text{-}MgCl_2]_n$ anionic building blocks are also formed, where magnesium chloride units are covalently bonded to aluminum halide species [10,20]. Indeed, δ-$MgCl_2$ is a particular covalent 1-D inorganic polymer endowed with a unique nature given by the presence of a strong covalent character of the Mg-Cl bonds [42]. The higher chemical reactivity of the "δ" phase with respect to the "α" and "β" phases finds its explanation by analyzing the short-range structural peculiarities of this material. In more detail, the Mg-Cl units that

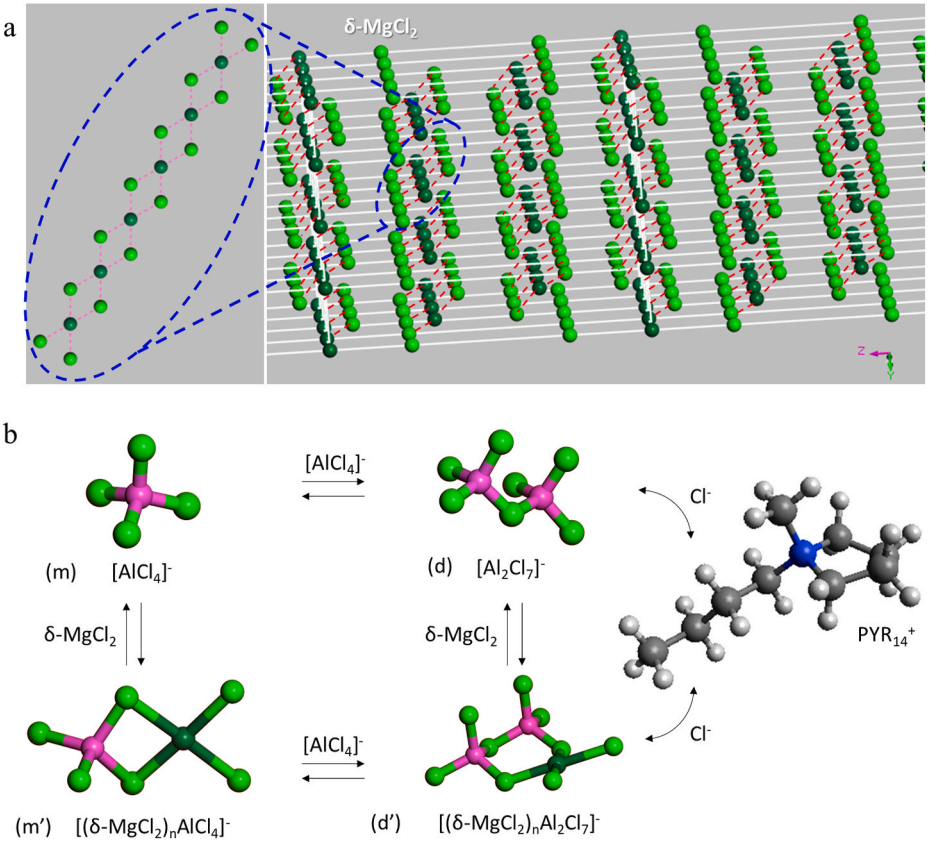

Scheme 1. Structure of the square-planar geometry of covalent δ-$MgCl_2$ (a). Ionic species composing the $[Pyr_{14}Cl/(AlCl_3)_{1.5}]/(\delta\text{-}MgCl_2)_x$ electrolytes (b). Color legend: C, H, N, Cl, Mg, Al. m and m' are the monomeric and d and d' the dimeric building blocks. m' and d' are the species catenated by $MgCl_2$ units.

compose δ-$MgCl_2$ consist of a disordered array of a large number of covalent $[MgCl_2]_n$ polymeric chains (Scheme 1a), where rhombohedral planar $MgCl_4$ edge-sharing units are distributed along these nanoribbons [42–44]. Pyrrolidinium cations (*i.e.*, Pyr_{14}^+) complete this picture. Summarizing, the possible ionic species present in the proposed $[Pyr_{14}Cl/(AlCl_3)_{1.5}]/(\delta\text{-}MgCl_2)_x$ electrolytes are: Pyr_{14}^+, $AlCl_4^-$, $Al_2Cl_7^-$, $[AlCl_4^-\text{-}MgCl_2]_n$ and $[Al_2Cl_7^-\text{-}MgCl_2]_n$ (Scheme 1b).

Within anionic catenated domains, a dynamic circular equilibrium exists between the monomeric (m) and dimeric (d) aluminum chloride, which can be modulated by varying: (i) the $AlCl_3$:$Pyr_{14}Cl$ molar ratio; (ii) the magnesium concentration; and (iii) the temperature. In this work, (ii) and (iii) conditions are explored, since (i) has been extensively investigated in the literature, albeit without δ-$MgCl_2$ [38,39,45,46]. This basic chemical equilibrium which triggers the dynamicity expressed by Scheme 1 can be summarized shortly by the following Equation (1):

$$Al_2Cl_7^- + Cl^- \leftrightarrow 2\ AlCl_4^- \quad (1)$$

In this case Cl^- is not free but involved in the neutralization of cationic domains aggregates (see Scheme 1). Several techniques have been proposed to investigate this equilibrium, of which the most accurate and quantitative are vibrational spectroscopies (*i.e.*, Raman and FT-IR) and solution-state ^{27}Al NMR. While the majority of the papers published in the literature agrees on which of the vibrational modes correspond specifically to the monomer or to the dimer [10,47–49], scientists are in disagreement in the NMR field [37–39,45,46]. In this work we try to shed light in this controversy, analyzing in high details the obtained results and offering a suitable explanation for the observed outcomes.

The results of solution-state ^{27}Al single-pulse NMR measurements are shown in Fig. 1. The two ^{27}Al signals are associated with the chloroaluminate anions, *i.e.*, the monomer $AlCl_4^-$ (m) and the dimer $Al_2Cl_7^-$ (d) building blocks. In accordance with the literature, the signal at *ca.* 103.2 ppm is attributed to the monomer $AlCl_4^-$, while the signal centered at *ca.* 97.0 ppm is attributed to the dimer $Al_2Cl_7^-$ [37–39,45,46]. As the $MgCl_2$ concentration is increased, the linewidths of these signals increased significantly. Interestingly, the chemical shifts of both the signals do not change significantly upon addition of δ-$MgCl_2$, indicating that their average molecular-environments are not changing appreciably over this range of investigated δ-$MgCl_2$ concentrations. To quantify these observations, the NMR signals were deconvoluted using DMFit to observe how the linewidth and relative areas of the two signals change as a function of temperature and Mg^{2+} concentration (Fig. 2, and Table S1 in the Supporting Information).

Quantitative analyses of deconvolutions of the ^{27}Al NMR spectra reveal that line broadening of the chloroaluminate species increases as a function of magnesium concentration in the electrolyte (x). In details, the linewidth associated with $AlCl_4^-$ increases to a greater degree than that of $Al_2Cl_7^-$. The increase in linewidths is due to greater electric quadrupolar relaxation rates, which dominate ^{27}Al NMR relaxation and are caused by stochastic fluctuations of the local ^{27}Al electric field gradients due to molecular motions. Two factors that could account for this increase are: (i) enhanced chemical exchange among the chloroaluminates and among the magnesium-chloroaluminate complexes; (ii) changes in molecular-level motions (*e.g.*, as manifested macroscopically by changes in viscosity) [39]. Regarding (i), faster rates of chemical exchange should result in faster relaxation and consequently larger linewidths upon Fourier transform of the NMR free induction decay. Regarding (ii), line broadening is expected to increase with increase in viscosity, since the electric quadrupolar relaxation rate depends upon fluctuations of molecular motions, such as reorientational correlation times that are correlated with the viscosity [39], and samples become more viscous as the concentration of δ-$MgCl_2$ is raised. As observed here, and consistent with similar systems reported in literature [38,39,45,48], $AlCl_4^-$ experiences significantly higher line broadening, with increase in δ-$MgCl_2$ concentration, ranging from 3931 Hz ($x = 0$) to 11382 Hz ($x = 0.146$). The broadening for $Al_2Cl_7^-$ ions increases to a lesser extent, from 765 Hz to only 2650 Hz. Ferrara et al. observed a similar increase in linewidth for $AlCl_4^-$ upon increasing $AlCl_3$ concentration in $AlCl_3$:

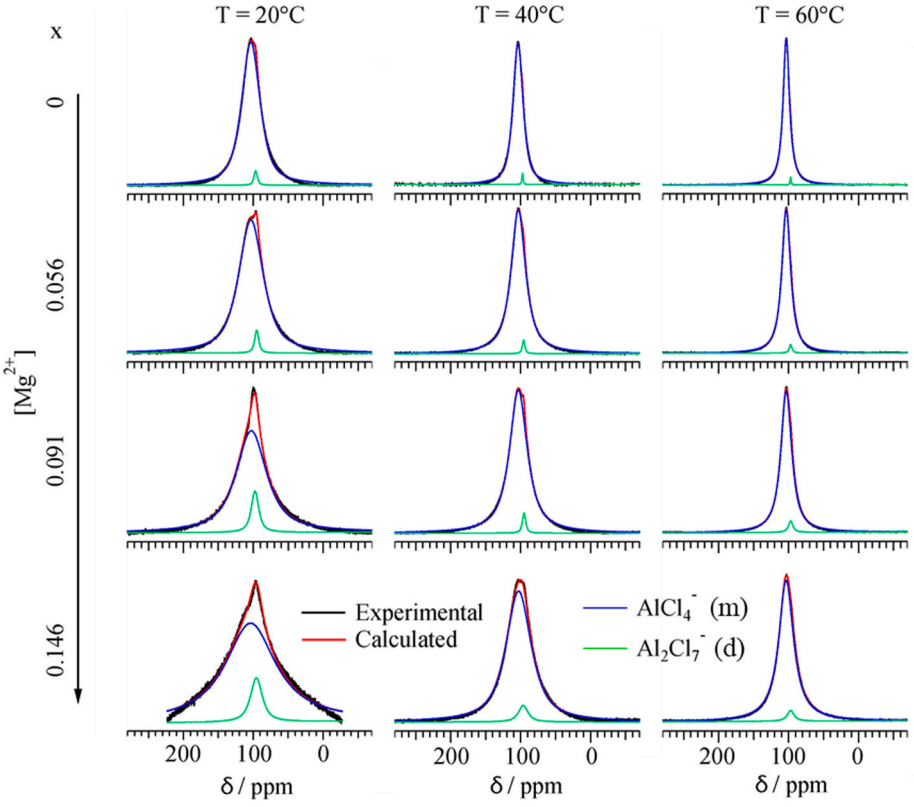

Fig. 1. Solution-state ^{27}Al single-pulse NMR spectra of $[Pyr_{14}Cl/(AlCl_3)_{1.5}]/(\delta\text{-}MgCl_2)_x$ samples as a function of magnesium concentration (x), lines, and temperature, columns. Black lines represent experimental data, while the fitted spectra are represented by red lines. The ^{27}Al signals associated with the monomer $AlCl_4^-$ and dimer $Al_2Cl_7^-$ are highlighted in blue and green, respectively. (For interpretation of the references to color in this figure legend, the reader is referred to the Web version of this article.)

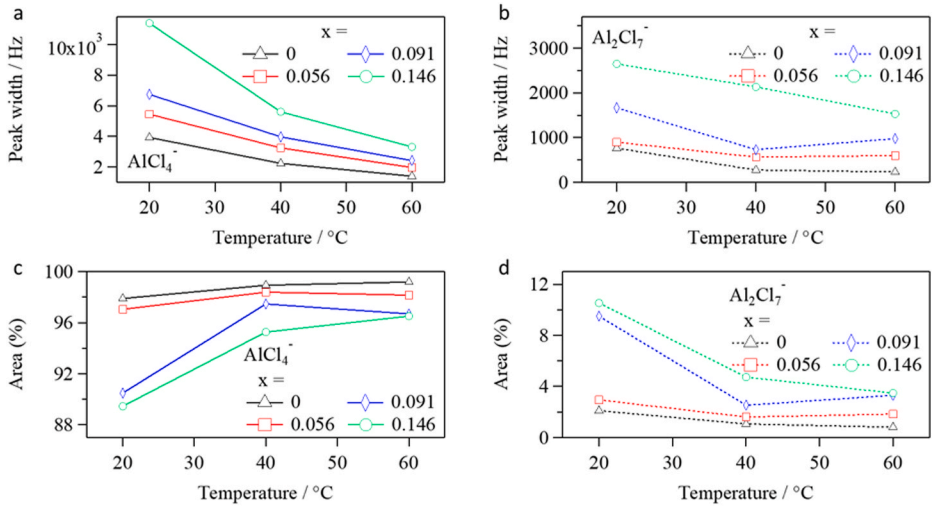

Fig. 2. Quantitative analyses of solution-state ^{27}Al single-pulse NMR spectra acquired as a function of temperature and δ-$MgCl_2$ content. Linewidths (full-width-half-max) for the monomer $AlCl_4^-$ (a) and dimer $Al_2Cl_7^-$ (b). Relative populations for the monomer $AlCl_4^-$ (c) and dimer $Al_2Cl_7^-$ (d).

[EMIm][Cl] electrolytes [38], indicating that the molecular environments and dynamics of $AlCl_4^-$ anions are more affected upon addition of $AlCl_3$, compared to $Al_2Cl_7^-$ [38]. Here, we hypothesize that the δ-$MgCl_2$ interacts to a greater extent with $AlCl_4^-$, compared to $Al_2Cl_7^-$, resulting in the rapid formation and disassociation of catenated $AlCl_4^-$/δ-$MgCl_2$ complexes, as well as affecting the $AlCl_4^-$ molecular mobility in anionic aggregates, giving rise to a faster relaxation and thus larger linewidths. Thus, it can be inferred from the ^{27}Al NMR measurements that the dynamics of $AlCl_4^-$ units into the catenated supramolecular anionic nanodomains are strongly affected by the addition of δ-$MgCl_2$.

Another important observation from Fig. 2 and Table S1 is that the relative area of the dimer $Al_2Cl_7^-$ at 97.0 ppm increases from 2.11% to 10.55% for $x = 0$ and 0.146, respectively. The value for $x = 0$ (*i.e.*, no δ-$MgCl_2$ inside) is shortly different to what it is observed for the $AlCl_3$/EMImCl system (*i.e.*, 9.1%) [38], indicating that the nature of the cation-cation interactions in cationic aggregates influences the Equilibrium (1). Moreover, the trend in the relative populations for the dimer as a function of δ-$MgCl_2$ concentration is in contrast to the Raman studies [20], where $Al_2Cl_7^-$ decreases with Mg-concentration. The integrated area for each chloroaluminate species depends upon the concentrations associated with Equilibrium (1) over the time scale of the NMR experiments. The rapid bond breaking between Al-Cl during chemical exchange within anionic catenated domains occurs on a timescale much faster than the timescale of NMR observations. Thus, the "*equilibrium*" concentrations measured by NMR spectroscopy may be different than that of Raman spectroscopy, due to: (i) rapid chemical exchange of the chloroaluminates; and (ii) the different time scales probed by the two techniques (*i.e.*, 10^{-12} *vs.* 10^{-3} s for Raman and NMR, respectively) [45]. As discussed above, addition of δ-$MgCl_2$ concentration further increases the intermolecular interactions between the δ-$MgCl_2$ and the monomer $AlCl_4^-$; this correlates with the reduced relative area for the monomer with increased Mg concentration. To

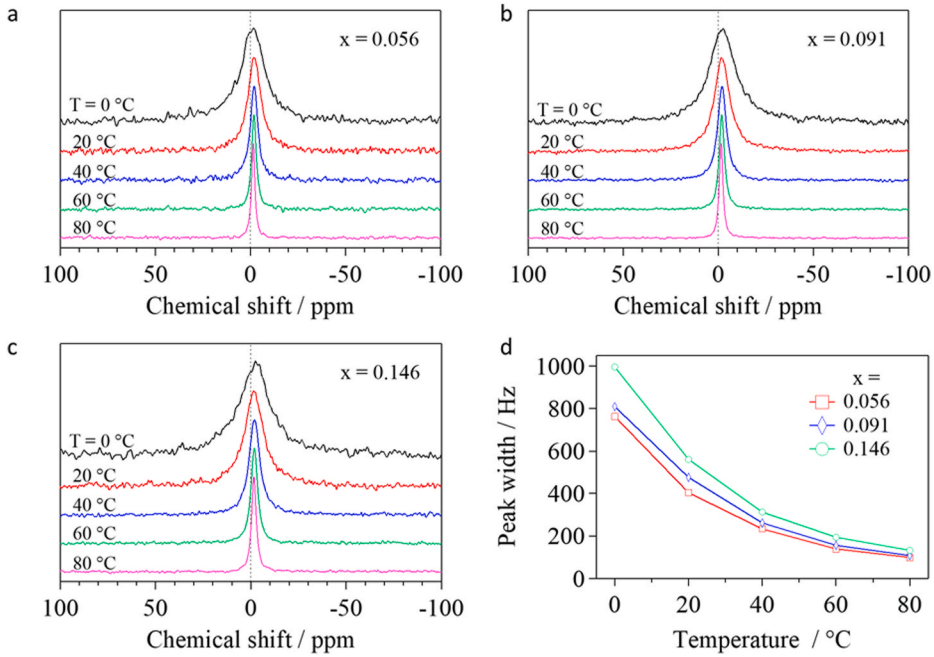

Fig. 3. Solution-state ^{25}Mg single-pulse NMR spectra of $[Pyr_{14}Cl/(AlCl_3)_{1.5}]/(δ\text{-}MgCl_2)_x$ samples as a function of temperature. Results for $x = 0.056$ (a), 0.091 (b) and 0.146 (c). Results of peak fitting to one component (Lorentzian line shape) as a function of temperature for the three samples (d).

summarize, from the solution-state ^{27}Al NMR measurements on [$Pyr_{14}Cl/(AlCl_3)_{1.5}$]/(δ-$MgCl_2$)$_x$ samples, we see the following observations: (i) linewidth of both chloroaluminates increases with increased Mg concentration, where the increase in linewidth is more significant for $AlCl_4^-$ than the $Al_2Cl_7^-$; and (ii) the relative area of $AlCl_4^-$ decreases with increase in Mg concentration. These two results further establish that δ-$MgCl_2$ interacts preferentially with the $AlCl_4^-$ anions.

Insights on magnesium species solvatation are given by ^{25}Mg NMR studies as a function of *x* and temperature. Results are shown in Fig. 3.

A single ^{25}Mg signal is detected, indicating that it is not possible to distinguish Mg-based species which are coordinated by the monomer $AlCl_4^-$ or by the dimer $Al_2Cl_7^-$, probably due to the fast chemical exchange between the two components. An alternative explanation is that, above the melting transition (see DSC analyses below), anionic nanodomains are composed by a random dispersion of the two chloroaluminate species. The ^{25}Mg chemical shift is between −1.0 and −2.5 ppm, indicating a very high solvating power for the proposed systems, foretelling a promising electrochemical activity. The ^{25}Mg linewidth (Fig. 3d) follows the same trend observed for ^{27}Al linewidths. Indeed, ^{25}Mg signals become modestly broader with increasing δ-$MgCl_2$, which is mainly attributed to the increasing in viscosity of the samples. This can be associated to the increase of the density of dynamic crosslinks inside the anionic catenated domains. In this case, slower molecular reorientation times (*i.e.* slower rotational dynamics), are expected, which are correlated to a decrease in the macroscopic viscosity of the material. In addition, narrow peaks are obtained when the temperature is increased, which indicates a corresponding increase in the mobility of Mg-based species and a decrease of the density of dynamic crosslinks inside the anionic aggregates.

Details on pyrrolidinium interactions established in the investigated materials are given by 1D ^{1}H NMR studies on *x* (see Fig. S2) and on temperature (see Fig. S3). In agreement with the literature [50,51], 1D ^{1}H NMR spectra of 1-butyl-1-methylpyrrolidinium ionic liquids show the presence of seven peaks attributed to the equivalent protons present in Pyr_{14}^+ cations, which are subjected to seven different chemical environments. An initial chemical shift decrease is observed on *x* (see Fig. S2), finally raising at high magnesium concentrations and showing a minimum for $x = 0.091$. The initial upfield shift reveals that the protons in Pyr_{14}^+ become more shielded on *x*, and their chemical shift value decreases as a consequence. This result can be explained considering that the additions of δ-$MgCl_2$ induce a tendency of a cluster-like structural evolution, resulting in a tighter structure in the complex network system and in the increase in the electron density around the ^{1}H nuclei of pyrrolidinium cations [52]. The final downfield shift can be attributed to the raise in viscosity at high magnesium concentrations. On T, all the electrolytes show a slight downfield shift of *ca.* 0.0026 ppm K^{-1} (see Fig. S3). These variable-temperature ^{1}H shifts are indicative of a decrease in electron density around the ^{1}H nuclei of Pyr_{14}^+, as the raise in temperature induces an increase of the distance between cation and anion domains [52]. Indeed, larger domains are expected when the temperature increases (see the Broadband Electrical Spectroscopy results discussed below). In addition, the extended size of cation aggregates induces a high electron delocalization, thus resulting in a deshielding effect on ^{1}H nuclei of Pyr_{14}^+.

3.2. Thermal properties

The thermal behavior of this family of IL-based electrolytes is further studied by differential scanning calorimetry (DSC) measurements (Fig. 4a).

DSC profiles reveal the presence of: (i) a glass transition (T_g) in a temperature range from −90 to −80 °C; (ii) three solid-solid endothermic transitions (T_{s3}, T_{s2}, and T_{s1}) at *ca.* −78, −76, and −50 °C; and (iii) a broad melting event (T_m) between −20 and 30 °C. T_g is attributed to an order-disorder event occurring into cationic aggregate domains. Indeed, in accordance with other studies [10,53,54], Pyr_{14}^+ cations tend to interact each other forming stacks interfaced with anion chloroaluminate catenated domains. This event on magnesium content gradually shifts toward higher temperatures (Fig. 4b). This effect is attributed to the ability of δ-$MgCl_2$ to modulate the interactions within the anion network domains influencing the equilibrium (1) between the different anionic repeat units, as previously discussed. Thus, the addition of δ-$MgCl_2$ results in a structural evolution (phase I → II, Fig. 4b) of anionic chloroaluminate catenated nanodomains, which perturbates the reorganization of the Pyr_{14}^+ cation stacks into cationic aggregate domains. These solid-solid transitions reveal that the proposed electrolytes at mesoscale are heterogeneous and consist of nanodomains characterized by a different conformational order [55–57]. It should be noticed that the T_s transitions characterizing these domains are detected at the same temperature regardless of *x*, thus demonstrating that these events depend only on the cationic aggregate domains and are not affected by the variations occurring in the anionic chloroaluminate catenated nanodomains. Finally, T_m is assigned to the melting transition of the IL (phase IV → V, Fig. 4b), which, as expected, depends on the concentration of magnesium species. Indeed, both the viscosity and the melting temperature are known to depend on the $AlCl_4^-/Al_2Cl_7^-$ composition [39]. On *x*, it is observed that T_m reaches a plateau when $x \geq 0.091$. This phenomenon can be explained considering that the increasing concentration of δ-$MgCl_2$ acts to extend the coordination network formed within the anion nanodomains. Reasonably, at $x = 0.091$ a maximum extension of the 3D network is achieved, thus limiting further increases in the melting temperature.

3.3. Electric response

[$Pyr_{14}Cl/(AlCl_3)_{1.5}$]/(δ-$MgCl_2$)$_x$ samples were extensively characterized by Broadband Electrical Spectroscopy (BES) [58–60] with the aim of: (i) studying the conductivity mechanisms responsible for the

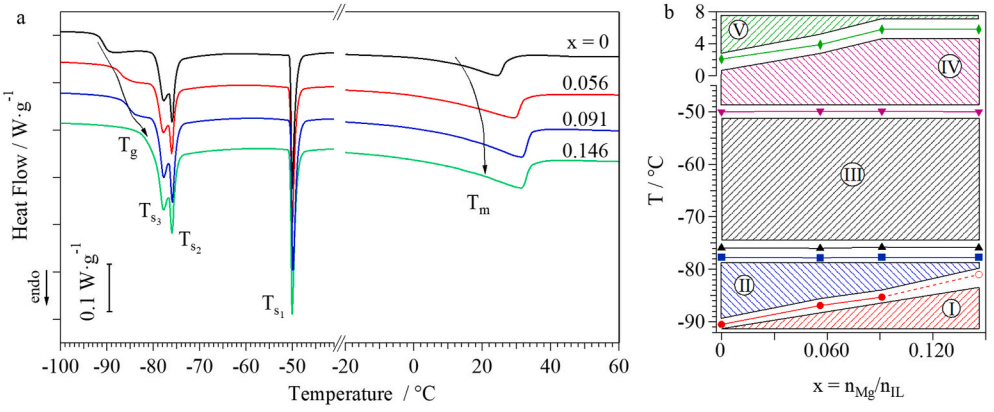

Fig. 4. DSC curves on δ-$MgCl_2$ concentration: $x = 0$ (black), 0.056 (red), 0.091 (blue), and 0.146 (green) (a). Thermal transitions are shown in the Figure: glass transition (T_g), solid-solid transitions ($T_{s,k}$, with k = 1, 2, and 3), and melting transition (T_m). Phase diagram of [$Pyr_{14}Cl/(AlCl_3)_{1.5}$]/(δ-$MgCl_2$)$_x$ electrolytes (b). Dependence of transition temperatures *vs.* *x* (n_{Mg}/n_{IL}). Each transition is identified by a different color: T_g (red circles), T_{s3} (blue squares), T_{s2} (black triangles), T_{s1} (violet revers triangles), and T_m (green diamonds). The different phases are indicated with roman numeral from "I" to "V". (For interpretation of the references to color in this figure legend, the reader is referred to the Web version of this article.)

long-range charge migration process; and (ii) highlighting the effects of the δ-$MgCl_2$ doping on the overall conductivity of the IL-based electrolytes. The obtained 3D tan δ spectra of the four investigated samples and the real conductivity results for the compound with $x = 0.091$ are shown, as an example, in Fig. 5a and Fig. 5b, respectively. The 2D BES curves for the four samples at all the temperatures and in terms of real and imaginary permittivity, conductivity and tan delta are reported in Figs. S4–S8 of the Supporting Information.

The electric response, in terms of both the imaginary and real components of the conductivity and permittivity, are analyzed with a suitable model, described by the following Equation (2) [58,61]:

$$\varepsilon_m^*(\omega) = -i\left(\frac{\sigma_0}{\omega\varepsilon_0}\right)^N + \sum_{k=1}^{n}\frac{\sigma_k(i\omega\tau_k)^{\gamma_k}}{i\omega\varepsilon_0\left[1+(i\omega\tau_k)^{\gamma_k}\right]} + \sum_{j=1}^{m}\frac{\Delta\varepsilon_j}{\left[1+(i\omega\tau_j)^{a_j}\right]^{b_j}} + \varepsilon_\infty \quad (2)$$

where $\varepsilon^*(\omega) = \varepsilon'(\omega) - i\varepsilon''(\omega)$, and $\sigma^*(\omega) = i\omega\varepsilon_0\varepsilon^*(\omega)$. The first term accounts for material conductivity at zero frequency (σ_0). N is the exponential factor of the direct current and ε_0 is is the absolute dielectric permittivity in vacuum. ε_∞ describes the electronic contribution, which is the permittivity of the material at infinite frequency. The second term is related to the interdomain and the electrode polarizations, where σ_k and τ_k are the conductivity and the relaxation times, respectively, associated with the k^{th} event. γ_k accounts for the broadening of the k^{th} polarization peak. The third term describes the dielectric relaxation phenomena in terms of generalized Havriliak-Negami functions [58,62]. τ_j, $\Delta\varepsilon$, α_j, and β_j are the relaxation time, dielectric strength, symmetric and antisymmetric shape parameters of the j^{th} relaxation event, respectively.

The conductivity values of all the polarization events, obtained by fitting the BES data in terms of real and imaginary components of complex permittivity, conductivity, and tan δ (see Figs. S4–S8 in the Supporting Information) using Equation (2), are plotted *vs.* T^{-1} in Fig. 6a.

Four different temperature regions are detected, which are delimited by the thermal transitions revealed by DSC measurements (T_m, T_{s1}, T_g). At temperatures higher than the glass transition temperature, five polarization phenomena can be observed (see Figs. 5b and 6a): (i) one electrode polarization (σ_{EP}), arising from the accumulation of charge at

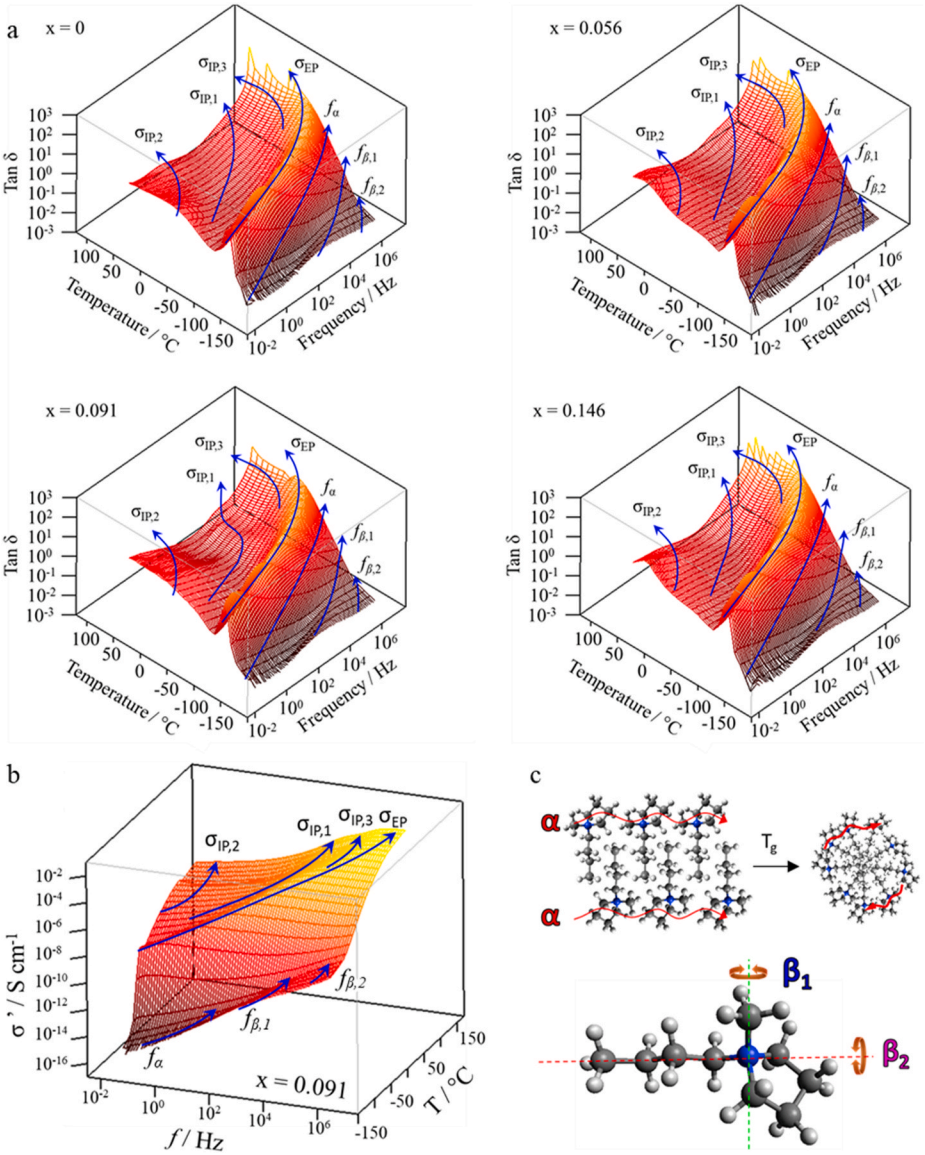

Fig. 5. 3D tan δ spectra as a function of frequency and temperature for the $[Pyr_{14}Cl/(AlCl_3)_{1.5}]/(\delta\text{-}MgCl_2)_x$ samples (a). 3D conductivity spectra as a function of frequency and temperature for the $[Pyr_{14}Cl/(AlCl_3)_{1.5}]/(\delta\text{-}MgCl_2)_{0.091}$ sample (b). Representative schematic of the dielectric relaxation events detected in the cation nanodomains for these materials (c).

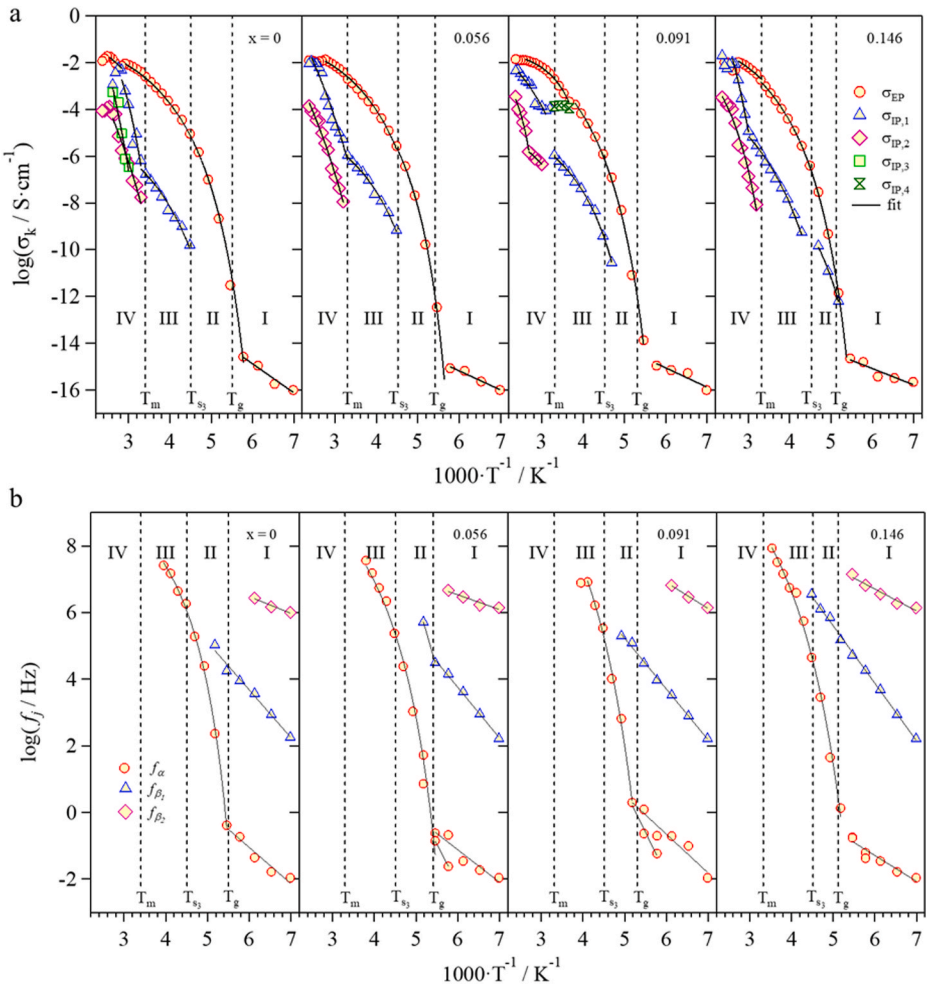

Fig. 6. Log σ_k *vs.* T^{-1} curves of each polarization for every sample (a). Log f_j *vs.* T^{-1} curves of each dielectric relaxation event for every sample (b). Temperature regions (I to IV) are identified considering the transition temperatures of each sample detected by MDSC measurements.

the interfaces between the sample and the electrode of the measuring cell [58]; and (ii) four different interdomain polarizations (σ_{IPk}, with $1 \leq k \leq 4$), attributed to the charge accumulation at the interfaces between nanodomains in bulk electrolyte with different permittivity [58]. The presence of these latter events, which are in agreement with NMR and DSC studies, allows to confirm that the proposed materials are heterogeneous at the mesoscale, and that they consist of pyrrolidinium-based cation nanoaggregates interacting with segregated chloroaluminate anion catenated nanodomains. At $T > T_g$, the conductivity values determined by the polarization events reveal a VTF-like behavior, demonstrating that the long-range charge migration processes occurring along these conductivity pathways is assisted by the host-medium relaxations of the IL aggregates. At $T < T_g$, σ_{EP} is the only detectable polarization phenomenon, contributing to the overall conductivity with a very low magnitude ($\sigma_T = \sigma_{EP} + \sum_{i=0}^{4} \sigma_{IP,i} \cong \sigma_{EP} < 10^{-14}$ S cm^{-1}). This is in accordance with the limited mobility of ions expected at these temperatures. Actually, in this latter region, the Arrhenius behavior exhibited by σ_{EP} *vs.* T^{-1} profile witnesses that the charge migration occurs through hopping events between neighboring coordination sites present within catenated anionic domains.

The dielectric relaxation frequency (f_j) values, obtained from the fitting of the 3D surfaces of the electric response of the electrolytes, are plotted as a function of temperature (T^{-1}) in Fig. 6b. At $T < T_g$, three dielectric relaxation events (f_j, with $1 \leq j \leq 3$) are detected: α-, β_1-and β_2-modes. The α relaxation is attributed to the diffusion of conformational states along the axis of staked interacting pyrrolidinium rings in cationic aggregated domains, while β_1 and β_2 are associated with the local rotational motion of Pyr_{14}^+ rod-like cations around the short and the long axis, respectively. A representative sketch of the dielectric relaxation events here detected for $[Pyr_{14}Cl/(AlCl_3)_{1.5}]/(\delta\text{-}MgCl_2)_x$ electrolytes is displayed in Fig. 5c. β_1 is revealed at a lower frequency with respect to β_2 due to the steric hindrance of the ordered butyl chains. At $T_g < T < T_m$, the α relaxation exhibits a Vogel Tammann Fulcher Hesse (VTFH) behavior, thus demonstrating that it is able to modulate efficiently the long-range charge migration processes within the studied electrolytes. It is interesting to notice that α and β_1/β_2 modes show on *x* the following behavior: (i) α dielectric relaxation shifts towards lower frequencies as the concentration of δ-$MgCl_2$ is raised. This means that the electrolytes with anionic domains richer in the $AlCl_4^-$ monomer species present an inhibited dynamic, thus raising the strength of interactions in the cation aggregate domains; (ii) on the other side, β_1-and β_2-modes are shifted on *x* at higher frequencies, thus demonstrating that the local anion-cation interactions are significantly influenced by the composition of the ionic segregated domains in the electrolytes. Indeed, the presence in catenated anionic domains of a higher concentration of $AlCl_4^-$ monomers, which is the species with the larger "*charge density*", act to strength the interactions with and between Pyr_{14}^+ units in cationic aggregates, thus modulating the dynamics of each single Pyr_{14}^+ molecule composing the cation aggregate.

To reveal how the host medium dynamics of cation and anion catenated domains influence the long-range charge migration events responsible of the conductivity pathways previously discussed, the

values of pseudo activation energies (E_a), determined by means of polarization phenomena, are correlated with the values of activation energies of the dielectric relaxations. This is carried out by fitting the curves reported in Fig. 6 by Arrhenius [58] or VTF/VTFH [63] equations. Results summarized in Fig. S9 of the Supporting Information are shown in the correlation map of Fig. 7a.

This map is useful in order to disclose the effect on conductivity phenomena (*i.e.*, σ_k) of the dielectric relaxation events (*i.e.*, f_j). Actually, conductivity pathways and dielectric relaxations are correlated when the relative marker lays on the dashed line in Fig. 7a, which indicate that the activation energy of the polarization phenomenon is consistent with that of the dielectric relaxation event. It can be observed that, for $x > 0$, β_1, detected in the low temperature regions (I and II), shows: i) the highest activation energy values ($27 < E_{a,\beta 1} < 34$ kJ mol^{-1}); and ii) is decoupled from the conductivity mechanism. On the other hand, in I and at $x \geq 0.056$, β_2 reveals an activation energy value which is correlated to that of σ_{EP}, thus indicating that in these conditions the relaxation mode of the long side chain of piled cations plays a crucial role in modulating the overall conductivity of materials. At $T > T_g$, in regions II - IV, the activation energy of σ_{EP} is perfectly correlated to the E_a of α-mode (*i.e. ca.* 9 kJ mol^{-1}). Therefore, at $T > T_g$, the diffusion of conformational states of Pyr_{14}^+ units along the stacking axis stimulates extended fluctuation waves of the cationic aggregates which effectively modulates and activates the long-range charge transfer mechanisms into anionic domains. In region IV, and at high magnesium concentrations, *i.e.*, at $x \geq 0.091$, a correlation between α and σ_{IP2} is also revealed. Moreover, on δ-$MgCl_2$ concentration, a decrease in the activation energy of σ_{EP}, and thus of the efficiency with which ionic species are exchanged at long-range distances within segregated anionic domains, is detected.

To achieve a better understanding of the conductivity mechanism, the dependence on temperature of the average charge migration distance (<r_k>) for the different percolation pathways is analyzed. <r_k> is determined by means of the Einstein-Smoluchowski Equation (3) [60]:

$$< r_k > (T_i) = \sqrt{6D_{\sigma_k}\tau_k} = \sqrt{\frac{6RT_i\sigma_k\tau_k}{Z_k^2 C_k F^2}} \quad (3)$$

where $D_{\sigma k}$ is the diffusion coefficient characterizing the k^{th} polarization, R the gas constant, T_i the temperature at which <r_k> is calculated, σ_k and τ_k are the conductivity and the relaxation time of the k^{th} polarization, respectively. Z_k and C_k are the charge and concentration, respectively, of the k^{th} species exchanged during the σ_k polarization. F is the Faraday constant. Results are shown in Fig. S10 of the Supporting Information. Generally, <r_k> increases on T, suggesting that larger clusters of segregated cation and anion domains are formed as the thermal energy is raised, owing to the increase of the strength and the density of the cation-cation and anion-anion interactions in the electrolytes. Therefore, <r_k> grows with *x*, indicating that the delocalization bodies (DBs) formed by aggregates of anions with different morphologies are increasing in size as the monomers $AlCl_4^-$ raise in concentration. This evidence corroborates the hypotheses above discussed in the 1D ^{1}H NMR studies. In this way, charge carriers are delocalized and can reach longer distances. In details, a delocalization body is a volume of the bulk electrolyte [64–67] where the active species are exchanged so fast between interacting species along the percolation pathways to be considered, in the time scale typical of macroscopic conductivity, delocalized. It is to be noted that <r_k> after doping of the electrolyte with δ-$MgCl_2$ slightly increases, thus witnessing that interactions between δ-$MgCl_2$ and chloroaluminate species act to improve the 3D network in both anion and cation segregated domains rising the size of the DBs. In addition, in correspondence of T_m a drop of <r_k> is revealed. This effect, which is mitigated in δ-$MgCl_2$-doped samples, confirms that an extended and strengthen coordination network is present in anionic domains after their doping with δ-$MgCl_2$.

3.4. Correlation between BES and PFG-NMR results

Despite the excellent level of accuracy in the BES studies, a complete understanding of the above described events can be achieved by clarify which of the elementary molecular relaxations is responsible for the detected BES phenomena. Indeed, BES is not element-specific since it detects only the charge relaxations and/or dipoles fluctuating events of host matrix. In this concern, PFG-NMR studies are employed to determine the local contribution of each ionic species to the overall charge diffusion (D) in the investigated electrolytes. In particular, ^{1}H self-diffusion coefficients are calculated to quantify the role of Pyr_{14}^+ ions in cationic domains and in the long-range charge migration process. Note that ^{25}Mg and ^{27}Al self-diffusion coefficients are difficult to study since the former has a low natural abundance and both nuclei experience significant quadrupole interactions leading to fast electric quadrupolar relaxation times. To determine the D values for all the samples at every temperature, the integrated intensities (*S*) are calculated from each experiment as a function of the applied gradient (*g*). Then, D coefficients are computed using a least-squares fitting of the Stejskal-Tanner Equation (4) [68]:

$$S = S_0 e^{-D(g\delta\gamma)^2\left(\Delta-\delta/3\right)} \quad (4)$$

where δ is the gradient pulse duration, Δ corresponds to the diffusion delay, and γ is the gyromagnetic ratio of the ^{1}H nucleus. Results of ^{1}H

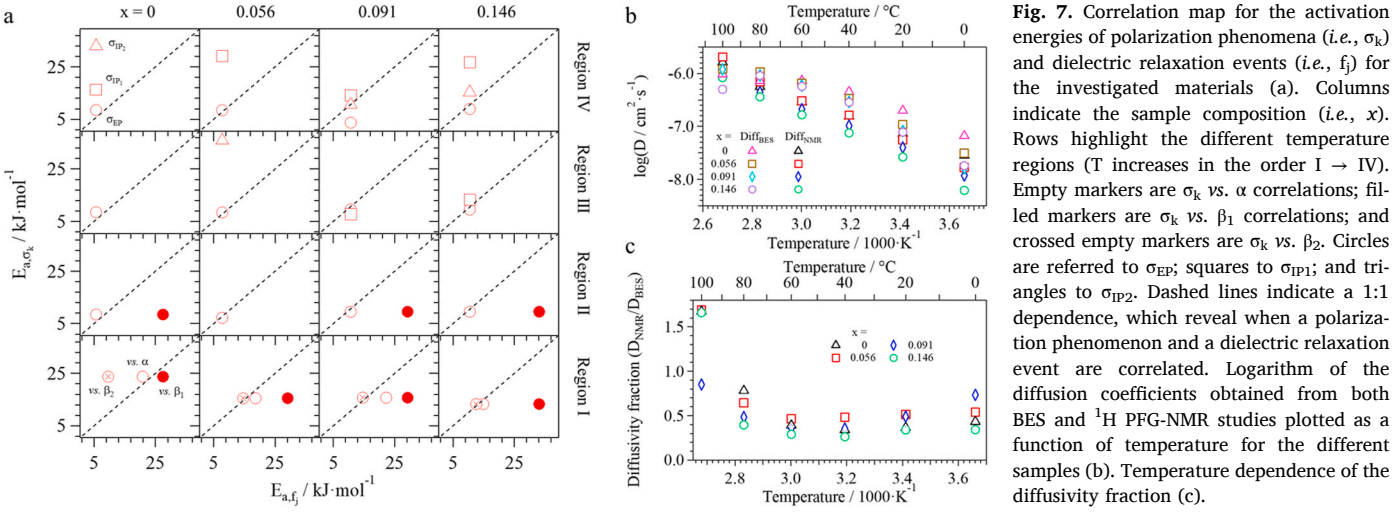

Fig. 7. Correlation map for the activation energies of polarization phenomena (*i.e.*, σ_k) and dielectric relaxation events (*i.e.*, f_j) for the investigated materials (a). Columns indicate the sample composition (*i.e.*, *x*). Rows highlight the different temperature regions (T increases in the order I → IV). Empty markers are σ_k *vs.* α correlations; filled markers are σ_k *vs.* β_1 correlations; and crossed empty markers are σ_k *vs.* β_2. Circles are referred to σ_{EP}; squares to σ_{IP1}; and triangles to σ_{IP2}. Dashed lines indicate a 1:1 dependence, which reveal when a polarization phenomenon and a dielectric relaxation event are correlated. Logarithm of the diffusion coefficients obtained from both BES and ^{1}H PFG-NMR studies plotted as a function of temperature for the different samples (b). Temperature dependence of the diffusivity fraction (c).

PFG-NMR studies on the different samples at various temperature are shown in Fig. S11. The dependence on T of D values thus obtained together with diffusion coefficients of the electrode polarization (*i.e.*, σ_{EP}) determined from BES analyses using Equation (3), are shown in Fig. 7b–c. Results are summarized in Table S2 of the Supporting Information.

The diffusion coefficient determined by both BES and ^{1}H PFG-NMR techniques is on the order of 10^{-8} cm^2 s^{-1} at low temperatures (*i.e.*, 0 °C) and rises up to 10^{-6} cm^2 s^{-1} at high temperatures (*i.e.*, 100 °C). Moreover, higher values of both D_{NMR} and D_{BES} are obtained for samples at low magnesium concentration, confirming that the ionic speciation modulates the local mobilities of ions as indicated by solution-state ^{27}Al and ^{25}Mg NMR linewidth analyses above. It is interesting to observe the difference of the diffusion coefficients obtained from BES studies with respect to those measured by ^{1}H PFG-NMR technique. Differences are easier to detect by calculating the diffusivity fraction, which is the ratio between D_{NMR} and D_{BES} (Fig. 7c). In general, this value is lower than 1, since ^{1}H PFG-NMR is detecting only the contribution of Pyr_{14}^{+} cations, while BES evaluates the total diffusivity of all the ions. Two important pieces of information are gained: (i) at $T > T_m$, both cation and anion species undergo a significant thermal activation, thus ionic nanoaggregates are dynamic and must not be considered as static agglomerates; and (ii) below 40 °C, the fraction value is lower than 0.5, indicating that a lower correlation between dynamics of cation and anion domains is present in these conditions. This signifies that the dynamics of cation aggregates are influencing less that of anion coordinated aggregates, thus confirming that long-range charge migration events take place owing to the exchange of ionic species between DBs formed by anion aggregate domains. A different thermal behavior is detected for the diffusivity fraction below and above 40 °C. In particular, at $T \leq 40$ °C the value is decreasing, while, at $T \geq 40$ °C, it increases. This can be easily explained considering the two effects of the temperature on the cation and anion aggregate domains of studied materials: (i) at $T \leq 40$ °C, the mobility into catenated anion domains is greater with respect to that of cation domains, since Pyr_{14}^{+} cations are strongly interacting along their stacking axis [10–13]; and (ii) at $T \geq 40$ °C, as the temperature is raised, the relaxation of interacting Pyr_{14}^{+} units along the stacking axis of cation aggregates, in accordance with f_α *vs.* T^{-1} curves of Fig. 7c, are significantly enhanced, thus improving the coupling between the dynamics of cation and anion aggregate domains [69]. Below 40 °C, the former effect induces a stronger contribution, thus the diffusivity fraction decreases with temperature. On the other hand, above 40 °C the coupling between cation and anion domains starts to dominate and an opposite trend is detected. Here, for the first time, these two complementary techniques (*i.e.*, ^{1}H PFG-NMR and BES spectroscopy) allowed to elegantly clarify: (i) how the effect of local dynamics influences the long-range charge migration mechanisms and thus the overall conductivity of very complex and heterogeneous (at a mesoscale level) systems such as those here investigated; (ii) to understand how the correlation effects between dynamics of cation and anion domains on temperature and composition influences the long-range charge migration phenomena; and (iii) that it is necessary to be very careful in complex electrolytes to assign the transference number on the basis of diffusion coefficients determined by only ^{1}H PFG-NMR. Indeed, in this case the investigated materials are characterized by quite high values of self-diffusion coefficient, both considering the solely Pyr_{14}^{+} cation and the whole ions composing the electrolytes. However, as previously discussed, the species responsible of the overall conductivity are present in anion domains. Here the overall conductivity takes place owing to the exchange of Al and Mg anion species between DBs which consist of 3D catenated magnesium chloroaluminate complexes. Therefore, excellent values of conductivity are achieved for the migration of Al and Mg chloro-complexes, which reach their maximum at medium temperatures (*ca.* 40 °C).

Concluding, the conductivity mechanism occurs by the long-range charge migration of Mg-coordinated chloroaluminate anion species that are exchanged between different delocalization bodies, and this mechanism is mainly assisted by the effect of the segmental motions of Pyr_{14}^{+} aggregates (α-mode). Both cations and anions, which compose the delocalization bodies, form nanoaggregates which are characterized by a high dynamicity. Indeed, charged species enter and exit these domains while they are fluctuating within the electrolytes. At medium-low temperatures ($T \leq 40$ °C) the conduction of Mg-coordinated chloroaluminate anion species is the main contribution to the total ionic current and it is weakly coordinated to the dynamics of Pyr_{14}^{+} cation aggregates. At higher temperatures ($T > 40$ °C) a strong correlation effect between Pyr_{14}^{+} cation aggregate dynamics and relaxations in catenated Al and Mg chloro-complexes domains is revealed, which enhances significantly the conductivity in materials. These effects are promoted by doping the electrolytes with δ-$MgCl_2$. Taken all together, these outcomes reveal the fundamental importance of understanding the conductivity mechanism to evaluate and predict the electrochemical performance of the electrolyte. Indeed, results here obtained clearly indicate that the properties and dynamics of the cation nanodomains (*i.e.*, diffusion of conformational states along the Pyr_{14}^{+} rings) are essential in order to trigger the exchange and conduction of active species (*i.e.*, Mg^{2+}/Al^{3+}). Furthermore, as the temperature is raised DBs increase in size, thus magnifying the delocalization effect of magnesium-chloroaluminate complexes in catenated supramolecular anionic domains. On the microscopic scale, this is demonstrated by the downfield shift of the peaks in the 1D ^{1}H NMR spectra (see Fig. S3) and the increasing average charge migration distance (see Fig. S10). The former is the result of the high electron delocalization in Pyr_{14}^{+} domains as they become larger with temperature. The latter arises from the infusion of neighboring domains allowing charges to be exchanged more efficiently. On the macroscopic scale, the larger DBs and coupling between cation and anion dynamics are revealed by the increase in the diffusion coefficient of active species, which is reflected by exceptional electrochemical activities (*e.g.*, fast kinetics, high exchange current densities, low ohmic drops and overpotentials) for these electrolytes [20].

4. Conclusion

In this report, the ion speciation, thermal properties, and conductivity mechanism of a novel family of IL-based electrolytes, with a general formula $[Pyr_{14}Cl/(AlCl_3)_{1.5}]/(\delta\text{-}MgCl_2)_x$, is studied for application in Al/Mg secondary batteries. Solution-state ^{27}Al single-pulse NMR measurements enable the chloroaluminate anionic species to be distinguished. Analysis of the ^{27}Al lineshapes as a function of temperature and δ-$MgCl_2$ content establish that the δ-$MgCl_2$ preferentially interacts with $AlCl_4^-$ anions, compared to the $Al_2Cl_7^-$ anions, which is consistent with similar trends revealed in the solution-state ^{25}Mg NMR measurements. Calorimetry studies reveal the presence of several thermal transition which arise from the structural reorganization of the cation and anion nanodomains. T_g and T_m transitions are modulated by the magnesium concentration, indicating that the ionic speciation has a role in the formation of the ionic nanoaggregates during these events. BES and ^{1}H PFG-NMR techniques are employed to shed light on the conductivity mechanism occurring in the studied materials from two different points of view. BES clearly confirm the presence of delocalization bodies which are composed by cation and anion nanoaggregates. Within DBs, Mg-chloroaluminate species (*i.e.*, the redox active species in these electrolytes) are exchanged between the coordination sites with a high kinetic and a low activation energy. Moreover, at $T > T_m$ the diffusion of conformational states along the Pyr_{14}^{+} rings (*i.e.*, α relaxation) facilitates the overall fluctuation of the cationic aggregates which effectively modulates and activates the charge transfer mechanism in anion domains. ^{1}H PFG-NMR allows to demonstrate that a coupling of dynamics in cation (*i.e.*, Pyr_{14}^{+} aggregates) and anion domains (*i.e.*, Mg and Al chloro-complexes) is present in these conditions. The coupling between these events contributes to enhance significantly the conductivity in materials. Taken all together, results provide a clear picture of ion

speciation, thermal behavior, and conductivity mechanism of this novel mixed Al/Mg metals family of electrolytes for secondary batteries.

Credit author statement

V.D.N., S.G.G. and R.J.M. conceived the idea for the project and planned the experiments. G.P. synthetized the electrolytes and performed the thermal analyses. K.V. executed the BES studies and elaborated the results. M.G. and L.F.O. carried out the ^{1}H PFG-NMR analyses and performed the calculations. A.J. executed the solution-state ^{27}Al NMR measurements and analyzed the data. B.I. performed the solution-state ^{25}Mg NMR analyses. All the authors discussed the results, conceived the conclusions and contributed to the final version of the manuscript. G.P. drafted the manuscript with the support and supervision of S.G.G., R.J.M. and V.D.N.

Declaration of competing interest

The authors declare that they have no known competing financial interests or personal relationships that could have appeared to influence the work reported in this paper.

Acknowledgements

This work was supported by the program "Budget Integrato per la Ricerca Interdipartimentale - BIRD 2018" of the University of Padova (protocol BIRD187913), by the "Centro Studi di Economia e Tecnica dell'Energia Giorgio Levi Cases" of the University of Padova and by the grant W911NF-21-1-0347 from the U.S. Army Research Office. The NMR work at Hunter College was supported by a grant #N00014-20-1-2186 from the U.S. Office of Naval Research. R.J.M and A.L.J. gratefully acknowledge the U.S. National Science Foundation for support via NSF CAREER award no. 1847552. The New York State Structural Biology Center is supported by grants from NYSTAR.

Appendix A. Supplementary data

Supplementary data to this article can be found online at https://doi.org/10.1016/j.jpowsour.2022.231084.

References

[1] D. Zhao, M. Wu, Y. Kou, E. Min, Ionic liquids: applications in catalysis, Catal. Today 74 (2002) 157–189.
[2] Z.S. Qureshi, K.M. Deshmukh, B.M. Bhanage, Applications of ionic liquids in organic synthesis and catalysis, Clean Technol. Environ. Policy 16 (2014) 1487–1513.
[3] S.P.M. Ventura, F.A. e Silva, M.V. Quental, D. Mondal, M.G. Freire, J.A. P. Coutinho, Ionic-liquid-mediated extraction and separation processes for bioactive compounds: past, present, and future trends, Chem. Rev. 117 (2017) 6984–7052.
[4] L. Fischer, T. Falta, G. Koellensperger, A. Stojanovic, D. Kogelnig, M. Galanski, R. Krachler, B.K. Keppler, S. Hann, Ionic liquids for extraction of metals and metal containing compounds from communal and industrial waste water, Water Res. 45 (2011) 4601–4614.
[5] X. Duan, J. Ma, J. Lian, W. Zheng, The art of using ionic liquids in the synthesis of inorganic nanomaterials, CrystEngComm 16 (2014) 2550–2559.
[6] G.A. Elia, U. Ulissi, S. Jeong, S. Passerini, J. Hassoun, Exceptional long-life performance of lithium-ion batteries using ionic liquid-based electrolytes, Energy Environ. Sci. 9 (2016) 3210–3220.
[7] B. Scrosati, J. Hassoun, Y.-K. Sun, Lithium-ion batteries. A look into the future, Energy Environ. Sci. 4 (2011) 3287–3295.
[8] G. Pagot, F. Bertasi, K. Vezzù, G. Nawn, G. Pace, A. Nale, V. Di Noto, Correlation between properties and conductivity mechanism in poly(vinyl alcohol)-based lithium solid electrolytes, Solid State Ionics 320 (2018) 177–185.
[9] D. Bansal, F. Cassel, F. Croce, M. Hendrickson, E. Plichta, M. Salomon, Conductivities and transport properties of gelled electrolytes with and without an ionic liquid for Li and Li-ion batteries, J. Phys. Chem. B 109 (2005) 4492–4496.
[10] F. Bertasi, C. Hettige, F. Sepehr, X. Bogle, G. Pagot, K. Vezzù, E. Negro, S. J. Paddison, S.G. Greenbaum, M. Vittadello, V. Di Noto, A key concept in magnesium secondary battery electrolytes, ChemSusChem 8 (2015) 3069–3076.
[11] F. Bertasi, F. Sepehr, G. Pagot, S.J. Paddison, V. Di Noto, Toward a magnesium-iodine battery, Adv. Funct. Mater. 26 (2016) 4860–4865.
[12] F. Bertasi, K. Vezzù, G. Nawn, G. Pagot, V. Di Noto, Interplay between structure and conductivity in 1-Ethyl-3-methylimidazolium tetrafluoroborate/(δ-$MgCl_2$)$_f$ electrolytes for magnesium batteries, Electrochim. Acta 219 (2016) 152–162.
[13] G. Pagot, F. Bertasi, K. Vezzù, F. Sepehr, X. Luo, G. Nawn, E. Negro, S.J. Paddison, V.D. Noto, Three-dimensional catenated 1-ethyl-3-methylimidazolium halotitanate ionic liquid electrolytes for electrochemical applications, Electrochim. Acta 246 (2017) 914–923.
[14] R. Dominko, J. Bitenc, R. Berthelot, M. Gauthier, G. Pagot, V. Di Noto, Magnesium batteries: current picture and missing pieces of the puzzle, J. Power Sources 478 (2020) 229027.
[15] G. Pagot, K. Vezzù, A. Nale, M. Fauri, A. Migliori, V. Morandi, E. Negro, V. Di Noto, Chrysalis-like graphene oxide decorated vanadium-based nanoparticles: an extremely high-power cathode for magnesium secondary batteries, J. Electrochem. Soc. 167 (2020), 070547.
[16] G. Zhu, M. Angell, C.-J. Pan, M.-C. Lin, H. Chen, C.-J. Huang, J. Lin, A.J. Achazi, P. Kaghazchi, B.-J. Hwang, H. Dai, Rechargeable aluminum batteries: effects of cations in ionic liquid electrolytes, RSC Adv. 9 (2019) 11322–11330.
[17] M.-C. Lin, M. Gong, B. Lu, Y. Wu, D.-Y. Wang, M. Guan, M. Angell, C. Chen, J. Yang, B.-J. Hwang, H. Dai, An ultrafast rechargeable aluminium-ion battery, Nature 520 (2015) 324–328.
[18] T. Gao, M. Noked, A.J. Pearse, E. Gillette, X. Fan, Y. Zhu, C. Luo, L. Suo, M. A. Schroeder, K. Xu, S.B. Lee, G.W. Rubloff, C. Wang, Enhancing the reversibility of Mg/S battery chemistry through Li^+ mediation, J. Am. Chem. Soc. 137 (2015) 12388–12393.
[19] Y. Ma, K. Shuai, L. Zhou, J. Wang, Q. Wang, Effect of Mg^{2+} and Mg^{2+}/Li^+ electrolytes on rechargeable magnesium batteries based on an erythrocyte-like CuS cathode, Dalton Trans. 49 (2020) 15397–15403.
[20] G. Pagot, K. Vezzù, S.G. Greenbaum, V. Di Noto, Hybrid twin-metal aluminum-magnesium electrolytes for rechargeable batteries, J. Power Sources 493 (2021) 229681.
[21] A. Stoppa, J. Hunger, R. Buchner, G. Hefter, A. Thoman, H. Helm, Interactions and dynamics in ionic liquids, J. Phys. Chem. B 112 (2008) 4854–4858.
[22] M.G. Del Pópolo, G.A. Voth, On the structure and dynamics of ionic liquids, J. Phys. Chem. B 108 (2004) 1744–1752.
[23] B. Wu, Y. Yamashita, T. Endo, K. Takahashi, E.W. CastnerJr, Structure and dynamics of ionic liquids: trimethylsilylpropyl-substituted cations and bis(sulfonyl) amide anions, J. Chem. Phys. 145 (2016) 244506.
[24] M. Jeyapandian, S. Lavina, S. Thayumanasundaram, H. Ohno, E. Negro, V. Di Noto, New hybrid inorganic–organic polymer electrolytes based on $Zr(O(CH_2)_3CH_3)_4$, glycerol and EMIm-TFSI ionic liquid, J. Power Sources 195 (2010) 341–353.
[25] J. Sangoro, C. Iacob, A. Serghei, S. Naumov, P. Galvosas, J. Kärger, C. Wespe, F. Bordusa, A. Stoppa, J. Hunger, R. Buchner, F. Kremer, Electrical conductivity and translational diffusion in the 1-butyl-3-methylimidazolium tetrafluoroborate ionic liquid, J. Chem. Phys. 128 (2008) 214509.
[26] S. Schrödle, G. Annat, D.R. MacFarlane, M. Forsyth, R. Buchner, G. Hefter, High frequency dielectric response of the ionic liquid N-methyl-N-ethylpyrrolidinium dicyanamide, Aust. J. Chem. 60 (2007) 6–8.
[27] S. Thayumanasundaram, M. Piga, S. Lavina, E. Negro, M. Jeyapandian, L. Ghassemzadeh, K. Müller, V. Di Noto, Hybrid inorganic–organic proton conducting membranes based on Nafion, SiO_2 and triethylammonium trifluoromethanesulfonate ionic liquid, Electrochim. Acta 55 (2010) 1355–1365.
[28] J.R. Sangoro, A. Serghei, S. Naumov, P. Galvosas, J. Kärger, C. Wespe, F. Bordusa, F. Kremer, Charge transport and mass transport in imidazolium-based ionic liquids, Phys. Rev. 77 (2008), 051202.
[29] F. Bertasi, G. Pagot, K. Vezzù, A. Nale, G. Pace, Y. Herve Bang, G. Crivellaro, E. Negro, V. Di Noto, Lithiated nanoparticles doped with ionic liquids as quasi-solid electrolytes for lithium batteries, Electrochim. Acta 307 (2019) 51–63.
[30] V. Di Noto, M. Piga, G.A. Giffin, S. Lavina, E.S. Smotkin, J.Y. Sanchez, C. Iojoiu, Influence of anions on proton-conducting membranes based on neutralized nafion 117, triethylammonium methanesulfonate, and triethylammonium perfluorobutanesulfonate. 2. electrical properties, J. Phys. Chem. C 116 (2012) 1370–1379.
[31] V. Di Noto, E. Negro, J.Y. Sanchez, C. lojoiu, Structure-relaxation interplay of a new nanostructured membrane based on tetraethylammonium trifluoromethanesulfonate ionic liquid and neutralized nation 117 for high-temperature fuel cells, J. Am. Chem. Soc. 132 (2010) 2183–2195.
[32] G.A. Giffin, A. Moretti, S. Jeong, K. Pilar, M. Brinkkötter, S.G. Greenbaum, M. Schönhoff, S. Passerini, Connection between lithium coordination and lithium diffusion in [Pyr_{120I}][FTFSI] ionic liquid electrolytes, ChemSusChem 11 (2018) 1981–1989.
[33] K. Pilar, A. Rua, S.N. Suarez, C. Mallia, S. Lai, J.R.P. Jayakody, J.L. Hatcher, J. F. Wishart, S. Greenbaum, Investigation of dynamics in BMIM TFSA ionic liquid through variable temperature and pressure NMR relaxometry and diffusometry, J. Electrochem. Soc. 164 (2017) H5189–H5196.
[34] C. Gainaru, E.W. Stacy, V. Bocharova, M. Gobet, A.P. Holt, T. Saito, S. Greenbaum, A.P. Sokolov, Mechanism of conductivity relaxation in liquid and polymeric electrolytes: direct link between conductivity and diffusivity, J. Phys. Chem. B 120 (2016) 11074–11083.
[35] O. Borodin, W.A. Henderson, E.T. Fox, M. Berman, M. Gobet, S. Greenbaum, Influence of solvent on ion aggregation and transport in PY_{15}TFSI ionic liquid-aprotic solvent mixtures, J. Phys. Chem. B 117 (2013) 10581–10588.
[36] S. Abbrent, S. Greenbaum, Recent progress in NMR spectroscopy of polymer electrolytes for lithium batteries, Curr. Opin. Colloid Interface Sci. 18 (2013) 228–244.

[37] J.S. Wilkes, J.S. Frye, G.F. Reynolds, Aluminum-27 and carbon-13 NMR studies of aluminum chloride-dialkylimidazolium chloride molten salts, Inorg. Chem. 22 (1983) 3870–3872.
[38] C. Ferrara, V. Dall'Asta, V. Berbenni, E. Quartarone, P. Mustarelli, Physicochemical characterization of $AlCl_3$-1-Ethyl-3-methylimidazolium chloride ionic liquid electrolytes for aluminum rechargeable batteries, J. Phys. Chem. C 121 (2017) 26607–26614.
[39] J.L. Gray, G.E. Maciel, Aluminum-27 nuclear magnetic resonance study of the room-temperature melt aluminum trichloride butylpyridinium chloride, J. Am. Chem. Soc. 103 (1981) 7147–7151.
[40] V. Di Noto, S. Lavina, D. Longo, M. Vidali, A novel electrolytic complex based on δ-$MgCl_2$ and poly(ethylene glycol) 400, Electrochim. Acta 43 (1998) 1225–1237.
[41] D. Massiot, F. Fayon, M. Capron, I. King, S. Le Calvé, B. Alonso, J.-O. Durand, B. Bujoli, Z. Gan, G. Hoatson, Modelling one- and two-dimensional solid-state NMR spectra, Magn. Reson. Chem. 40 (2002) 70–76.
[42] M. Vittadello, P.E. Stallworth, F.M. Alamgir, S. Suarez, S. Abbrent, C.M. Drain, V. Di Noto, S.G. Greenbaum, Polymeric δ-$MgCl_2$ nanoribbons, Inorg. Chim. Acta. 359 (2006) 2513–2518.
[43] V. Di Noto, S. Bresadola, New synthesis of a highly active δ-$MgCl_2$ for $MgCl_2/TiCl_4/AlEt_3$ catalytic systems, Macromol. Chem. Phys. 197 (1996) 3827–3835.
[44] V. Di Noto, R. Zannetti, M. Vivani, C. Marega, A. Marigo, S. Bresadola, $MgCl_2$-supported Ziegler-Natta catalysts: a structural investigation by X-ray diffraction and Fourier-transform IR spectroscopy on the chemical activation process through $MgCl_2$-ethanol adducts, Makromol. Chem. 193 (1992) 1653–1663.
[45] S. Takahashi, M.-L. Saboungi, R.J. Klingler, M.J. Chen, J.W. Rathke, Dynamics of room-temperature melts: nuclear magnetic resonance measurements of dialkylimidazolium haloaluminates, J. Chem. Soc., Faraday Trans. 89 (1993) 3591–3595.
[46] Z. Cerny, J. Machacek, J. Fusek, B. Casensky, O. Kriz, D. Tuck, ^{27}Al NMR studies of the hydrolysis of aluminium(III) chloride in non-aqueous media, Inorg. Chim. Acta. 300–302 (2000) 556–564.
[47] C.J. Dymek, J.S. Wilkes, M.A. Einarsrud, H.A. Øye, Spectral identification of $Al_3Cl_{10}^-$ in 1-methyl-3-ethylimidazolium chloroaluminate molten salt, Polyhedron 7 (1988) 1139–1145.
[48] S. Takahashi, L.A. Curtiss, D. Gosztola, N. Koura, M.-L. Saboungi, Molecular orbital calculations and Raman measurements for 1-Ethyl-3-methylimidazolium chloroaluminates, Inorg. Chem. 34 (1995) 2990–2993.
[49] K. Nakamoto, Infrared and Raman Spectra of Inorganic and Coordination Compounds - Part A: Theory and Applications in Inorganic Chemistry, sixth ed., Wiley, Hoboken, New Jersey, 2009.
[50] T.A. Fadeeva, P. Husson, J.A. DeVine, M.F.C. Gomes, S.G. Greenbaum, E. W.C Jr., Interactions between water and 1-butyl-1-methylpyrrolidinium ionic liquids, J. Chem. Phys. 143 (2015), 064503.
[51] F. Castiglione, G. Raos, G. Battista Appetecchi, M. Montanino, S. Passerini, M. Moreno, A. Famulari, A. Mele, Blending ionic liquids: how physico-chemical properties change, Phys. Chem. Chem. Phys. 12 (2010) 1784–1792.
[52] T.-Y. Wu, S.-G. Su, Y.-H. Wang, Y.-C. Lin, J.-K. Chang, C.-W. Kuo, I.W. Sun, Diffusion coefficients, spin-lattice relaxation times, and chemical shift variations of NMR spectra in LiTFSI-doped ether- and allyl-functionalized dicationic ionic liquids, J. Taiwan Inst. Chem. Eng. 60 (2016) 138–150.
[53] E. Gómez, N. Calvar, Á. Domínguez, E.A. Macedo, Thermal behavior and heat capacities of pyrrolidinium-based ionic liquids by DSC, Fluid Phase Equil. 470 (2018) 51–59.
[54] C.S. Stefan, D. Lemordant, P. Biensan, C. Siret, B. Claude-Montigny, Thermal stability and crystallization of N-alkyl-N-alkyl′-pyrrolidinium imides, J. Therm. Anal. Calorim. 102 (2010) 685–693.
[55] W.A. Henderson, V.G. Young, S. Passerini, P.C. Trulove, H.C. De Long, Plastic phase transitions in N-ethyl-N-methylpyrrolidinium bis(trifluoromethanesulfonyl) imide, Chem. Mater. 18 (2006) 934–938.
[56] D.R. MacFarlane, P. Meakin, J. Sun, N. Amini, M. Forsyth, Pyrrolidinium imides:A new family of molten salts and conductive plastic crystal phases, J. Phys. Chem. B 103 (1999) 4164–4170.
[57] W.A. Henderson, S. Passerini, Phase behavior of ionic liquid-LiX mixtures: pyrrolidinium cations and TFSI -anions, Chem. Mater. 16 (2004) 2881–2885.
[58] V. Di Noto, G.A. Giffin, K. Vezzù, M. Piga, S. Lavina, Broadband dielectric spectroscopy: a powerful tool for the determination of charge transfer mechanisms in ion conductors, in: Solid State Proton Conductors: Properties and Applications in Fuel Cells, John Wiley & Sons, Chichester, U.K., 2012, pp. 109–183.
[59] V. Di Noto, M. Vittadello, K. Yoshida, S. Lavina, E. Negro, T. Furukawa, Broadband dielectric and conductivity spectroscopy of Li-ion conducting three-dimensional hybrid inorganic–organic networks as polymer electrolytes based on poly(ethylene glycol) 400, Zr and Al nodes, Electrochim. Acta 57 (2011) 192–200.
[60] G. Pagot, S. Tonello, K. Vezzù, V. Di Noto, A new glass-forming electrolyte based on lithium glycerolate, Batteries 4 (2018) 41.
[61] V. Di Noto, M. Vittadello, S.G. Greenbaum, S. Suarez, K. Kano, T. Furukawa, A new class of lithium hybrid gel electrolyte systems, J. Phys. Chem. B 108 (2004) 18832–18844.
[62] S. Kitajima, F. Bertasi, K. Vezzù, E. Negro, Y. Tominaga, V. Di Noto, Dielectric relaxations and conduction mechanisms in polyether–clay composite polymer electrolytes under high carbon dioxide pressure, Phys. Chem. Chem. Phys. 15 (2013) 16626–16633.
[63] G. Tammann, W. Hesse, Die Abhängigkeit der Viscosität von der Temperatur bie unterkühlten Flüssigkeiten, Z. Anorg. Allg. Chem. 156 (1926) 245–257.
[64] K. Vezzù, G. Nawn, G. Pagot, E. Negro, A. Nale, Y.H. Bang, F. Conti, G. Cavinato, V. Di Noto, Relaxation phenomena and conductivity mechanisms in anion-exchange membranes derived from polyketone, Electrochim. Acta 319 (2019) 253–263.
[65] G. Nawn, K. Vezzù, F. Bertasi, G. Pagot, G. Pace, F. Conti, E. Negro, V. Di Noto, Electric response and conductivity mechanism in H_3PO_4-doped polybenzimidazole-4N−HfO_2 nanocomposite membranes for high temperature fuel cells, Electrochim. Acta 228 (2017) 562–574.
[66] V. Di Noto, M. Piga, G.A. Giffin, K. Vezzù, T.A. Zawodzinski, Interplay between mechanical, electrical, and thermal relaxations in nanocomposite proton conducting membranes based on nafion and a [(ZrO_2) (Ta_2O_5)$_{0.119}$] core-shell nanofiller, J. Am. Chem. Soc. 134 (2012) 19099–19107.
[67] G.A. Giffin, G.M. Haugen, S.J. Hamrock, V. Di Noto, Interplay between structure and relaxations in perfluorosulfonic acid proton conducting membranes, J. Am. Chem. Soc. 135 (2013) 822–834.
[68] E.O. Stejskal, J.E. Tanner, Spin diffusion measurements: spin echoes in the presence of a time-dependent field gradient, J. Chem. Phys. 42 (1965) 288–292.
[69] D. Morales, R.E. Ruther, J. Nanda, S. Greenbaum, Ion transport and association study of glyme-based electrolytes with lithium and sodium salts, Electrochim. Acta 304 (2019) 239–245.